


Article

# In-Situ Transformation of Li-ABW Zeolites Based on Li-Geopolymer

Huaiyuan Dou , Quan Ye, Yan He and Xuemin Cui \*

Guangxi Key Lab of Petrochemical Resource Processing and Process Intensification Technology, School of Chemistry and Chemical Engineering, Guangxi University, Nanning 530004, China

\* Correspondence: cuixm@gxu.edu.cn

**Abstract:** Lithium batteries, as energy storage devices, are playing an increasingly important role in human society. As a result of the low safety of the liquid electrolyte in batteries, more attention has been paid to solid electrolytes. Based on the application of lithium zeolite in a Li-air battery, a non-hydrothermal converted lithium molecular sieve was prepared. In this paper, in-situ infrared spectroscopy, together with other methods, was used to characterize the transformation process of geopolymer-based zeolite. The results showed that Li/Al = 1.1 and 60 °C were the best transformation conditions for the Li-ABW zeolite. On this basis, the geopolymer was crystallized after 50 min of reaction. This study proves that the formation of geopolymer-based zeolite occurs earlier than the solidification of the geopolymer and shows that the geopolymer is a good precursor for zeolite conversion. At the same time, it comes to the conclusion that the formation of zeolite will have an impact on the geopolymer gel. This article provides a simple preparation process for lithium zeolite, explores the preparation process and mechanism, and provides a theoretical basis for future applications.

**Keywords:** in-situ infrared spectroscopy; non-hydrothermal transportation; Li-geopolymer; Li-ABW



**Citation:** Dou, H.; Ye, Q.; He, Y.; Cui, X. In-Situ Transformation of Li-ABW Zeolites Based on Li-Geopolymer. *Gels* **2023**, *9*, 392. <https://doi.org/10.3390/gels9050392>

Academic Editor: Dirk Kuckling

Received: 27 March 2023

Revised: 16 April 2023

Accepted: 4 May 2023

Published: 9 May 2023



**Copyright:** © 2023 by the authors. Licensee MDPI, Basel, Switzerland. This article is an open access article distributed under the terms and conditions of the Creative Commons Attribution (CC BY) license (<https://creativecommons.org/licenses/by/4.0/>).

## 1. Introduction

Due to the problems of insufficient electrochemical and thermal stability, low ion selectivity, and poor safety in liquid electrolytes [1], solid electrolytes [2–4] that can replace liquid electrolytes have received increasing attention. Similarly, new energy vehicles have stricter safety requirements [5–7]. The International Energy Agency estimates that the global sales of electric vehicles will reach 245 million in 2030, on the basis of the current and expected future policies, with corresponding annual sales growth of approximately 41% and a stock value of USD 13 billion and USD 130 billion [8]. Thus, research on better solid electrolyte materials has become more significant.

Chi et al. [9] proposed a zeolite electrolyte solid-state Li-air battery. The LiX zeolite membrane is obtained by replacing the Li<sup>+</sup> of the dense FAU molecular sieve membrane with Na<sup>+</sup>. However, from the perspective of the preparation process consumption, this requires a long time period for a hydrothermal reaction and multiple ion exchange to occur [10–13]. Therefore, it is more important to find a lithium zeolite with low energy cost and simple technology.

Metakaolin (MK)-based Geopolymer [14–17] has a suitable element ratio that can be crystallized and converted into zeolite in situ under certain conditions of temperature and pressure. Therefore, it is often used as the raw material of low-silicon zeolite. In addition, the advantages of this in-situ zeolite are that the geopolymer provides strength and stability, while the zeolite provides a high surface area, porosity, and adsorption [18].

The in-situ conversion of zeolite from geopolymers and its application have been widely studied [19–21]. For example, Ye et al. [22] used NaOH to activate MK foaming to prepare geopolymer microspheres and transform them into NaA molecular sieves in

situ for CO<sub>2</sub> hydrogenation catalyzed by supported Ni, Pt, and Pd. Guan et al. [23] used sodium silicate as the activator in the preparation of MK-based geopolymer; then, the faujasite zeolite was prepared through hydrothermal reaction in a 2 mol/L NaOH solution at 90 °C for 24 h. The compressive strength can reach 11.7 Mpa. Wei et al. [24] obtained the crystallinity of 62.42% cubic zeolite microspheres after curing the MK with 11 M sodium hydroxide at 85 °C for 72 h, and its adsorption capacity of Pb<sup>2+</sup> was up to 308.3 mg/g. Such an approach manifests sustainability benefits as the synthesis of geopolymers is more energy- and time-efficient compared to conventional zeolite synthesis [18].

In terms of energy, compared with synthetic zeolite, the activation energy corresponding to the formation of low-silica zeolite was reduced by the geopolymer gel. In other words, the geopolymerization further ordered the arrangement of Si-O tetrahedron and Al-O tetrahedron and formed the microcrystals that would be seeds [25] in the in-situ transformation. Therefore, theoretically speaking, the crystallization of geopolymers should be milder. In addition, a NaA molecular sieve can be prepared using a MK-based geopolymer with a certain Na/Al ratio under non-hydrothermal conditions below 70 °C in the study of in-situ low-silicon zeolite [26]. However, crystallization of geopolymer usually requires hydrothermal conditions, which are no different from the conditions of artificial zeolite.

Lithium, the first element of the alkali metal group, has two hydroxides, both of which are strong bases that are rarely used in the activation of geopolymers because of their low solubility. In the relevant literature reports, lithium hydroxide (monohydrate) is generally used as the raw material of the in-situ lithium zeolite transformation precursor and as the solute of the hydrothermal solution. In general, the vast majority of lithium zeolite (almost zeolite ABW) prepared using the geopolymeric method [27–31] have been obtained from the hydrothermal reaction of solidified geopolymer blocks. However, the crystallization of a lithium-based geopolymer can be conducted at a low temperature and in a short amount of time, even without hydrothermal processes. In this work, a low-temperature and non-hydrothermal Li-ABW molecular sieve was successfully prepared. The optimum technology was explored by controlling different Li/Al ratios and curing (transformation) temperatures and times. The formation of Li-ABW was characterized using in-situ infrared spectroscopy. This work provides a simple preparation process for lithium zeolite, explores the preparation process and mechanism, and provides a theoretical basis for future applications.

## 2. Results and Discussion

### 2.1. XRD Analysis

As no hydrothermal reaction was required, only the effects of the Li/Al, temperature, and time on the crystallization of the lithium-based geopolymer have been investigated. The results were as follows.

The curing condition was controlled at 60 °C for 24 h. Figure 1a shows the transformation of the geopolymer under different quantities of LiOH·H<sub>2</sub>O addition. What can be confirmed is that the characteristics diffraction peaks of all the crystallized samples at 2θ are 13.78°, 17.24°, 20.51°, 20.96°, 28.29°, and 29.65°, which are consistent with the standard card of Li-ABW zeolite (JPCDS card No. 41-0554). The crystallization rate shows a clear trend of first increasing and then decreasing with the increase in the Si/Al ratio. Generally speaking, when the amount of alkali added is small, the formation of geopolymer gel is insufficient, leading to a reduction in the raw materials of the subsequent molecular sieves, which causes a decrease in the output of zeolite. When Li/Al = 0.6, there were only weak diffraction peaks, and the sample was still an amorphous aluminosilicate gel, which can be proven. Similarly, if the alkalinity is too high, the zeolite microcrystals in the geopolymerization are dissolved by the high alkali slurry. However, when the activator is lithium hydroxide, its contribution is different from that of other strong bases. The saturation concentration of lithium hydroxide solution at normal atmospheric conditions is about 5.39 mol/L due to the solubility problem. It can be seen that the amount of activator added in the crystallization alkalinity interval of the lithium geopolymer is supersaturated, which leads to a constant

pH in the geopolymeric reaction for a period of time. In addition, there will be water formation and evaporation in the reaction itself. Therefore, the amount of water added is only related to whether geopolymer form slurries. Figure 1b also proves that when the  $\text{H}_2\text{O}/\text{Li}_2\text{O}$  was increased by one, the diffraction peak intensity was significantly weakened. This oversaturation of the alkali can also explain the phenomenon of the intensity of the XRD diffraction peak being more or less consistent in several regions. In summary, the effect of these alkalinity levels on the transformation may be attenuated by the saturated nature of the activator, which is essentially the balance between the contribution of  $\text{Li}^+$  and the microcrystal induction effect and the influence of the gel amount on the crystallization.

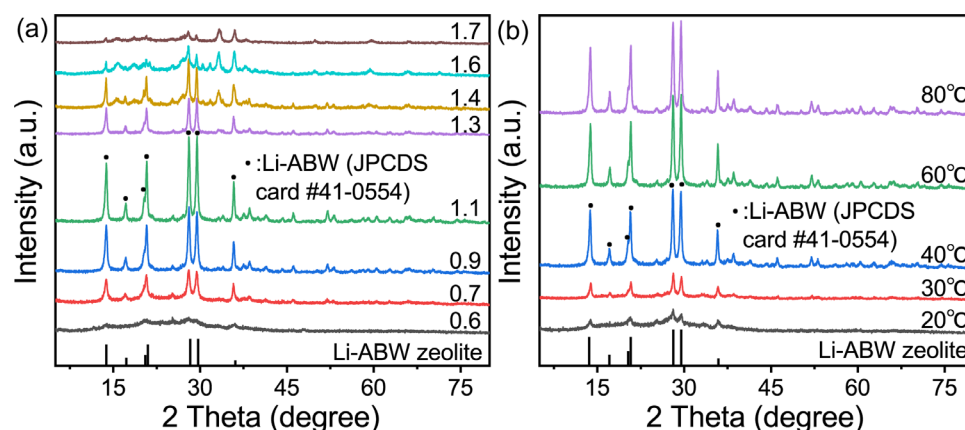


**Figure 1.** XRD patterns of effects of (a) Li/Al curing at 60 °C for 24 h and (b) temperature curing for 24 h when Li/Al = 1.1.

Thus, the Li/Al ratio was fixed at 1.1, while the curing time remained at 24 h. Figure 1b shows the transformation of the lithium-based geopolymer at different temperatures. It can be seen that no molecular sieve is generated when curing below 30 °C. Then, with the temperature reaching 60 °C, the crystallinity of the sample gradually increases. When the temperature is higher than 60 °C, the intensity of the Li-ABW characteristic diffraction peak is basically unchanged, which can be judged as the best formation temperature for lithium zeolite. However, for each sample, the crystallization limit is subject to its original composition; that is, compared with the curing time and temperature, the transformation of the geopolymer in this experiment mainly depended on the Li/Al ratio of the raw materials. Table 1 lists the comparisons between the preparation process of the Li-ABW in this experiment and other experiments. Compared with the process proposed in this chapter, it can be seen that the in-situ conversion method of geological polymers has great advantages, and geological polymers are excellent precursors of zeolite.

**Table 1.** Comparison of the preparation process of Li-ABW with other experiments.

Starting Mixture	Temperature (°C)	Total Time (h)	References
MK-LiOH·H <sub>2</sub> O-H <sub>2</sub> O	60	24	This work
CFBFA-LiOH·H <sub>2</sub> O-H <sub>2</sub> O	180	24	[27]
FA-LiOH·H <sub>2</sub> O-H <sub>2</sub> O	160	16	[28]
FA-LiOH-H <sub>2</sub> O	180	24	[30]
FACs-LiOH·H <sub>2</sub> O-H <sub>2</sub> O	180	24	[31]

## 2.2. SEM Analysis

Figure 2 shows the SEM images of the geopolymer and Li-ABW zeolite. The fixed curing time is 24 h. Figure 2a shows Li/Al = 1.1, curing at 20 °C. The clear gel structure, incompletely reacted metakaolin particulates, and a small amount of lithium zeolite microcrystals, which will become the nucleus of the subsequent gel transformation, can be

seen. When the curing temperature rose, as shown in Figure 2b, with  $\text{Li}/\text{Al} = 0.9$  and curing at  $40^\circ\text{C}$ , due to the relatively insufficient amount of activator, large MK particles remained and zeolite crystals grew on its surface. Figure 2c shows the condition under  $\text{Li}/\text{Al} = 0.6$  and  $T = 60^\circ\text{C}$ , at which the alkalinity is relatively insufficient. Compared with low-temperature curing, the amount of gel increases at high temperatures, and the unreacted raw materials basically disappear. However, there is no zeolite microcrystalline structure in the image. Accordingly, in Figure 2d, with  $\text{Li}/\text{Al} = 1.7$  and  $T = 60^\circ\text{C}$ , the gel was relatively denser and the only crystal phase in the image may be an unreacted  $\text{LiOH}\cdot\text{H}_2\text{O}$  solid, which can also prove the influence of the alkalinity on the conversion of the geopolymer, as mentioned above.

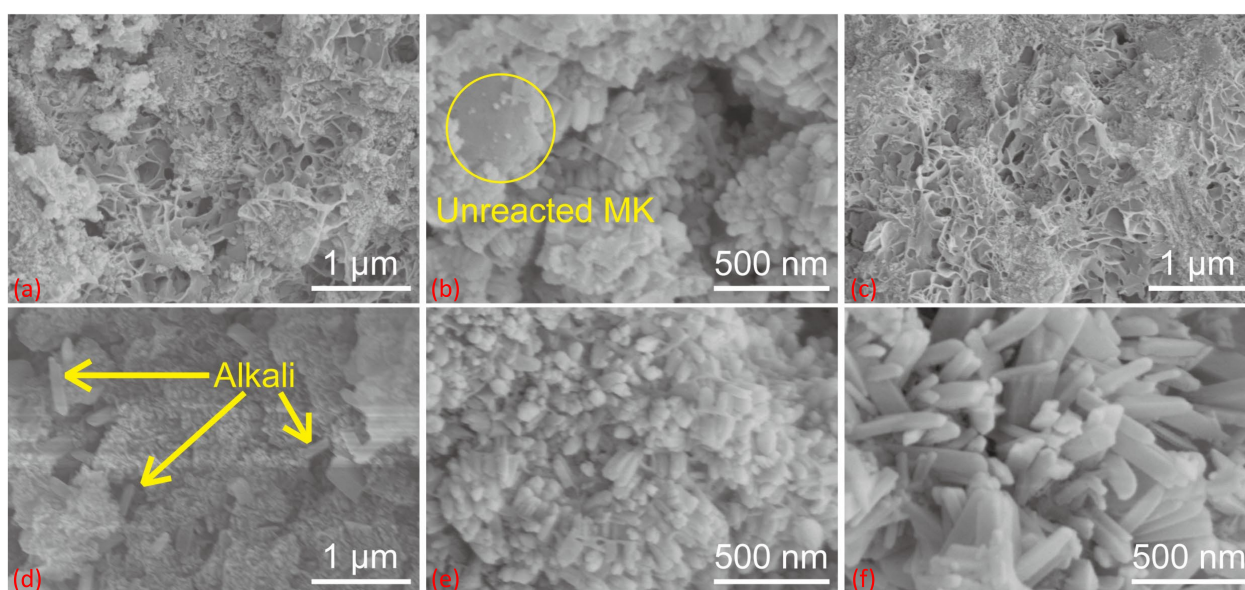


**Figure 2.** SEM patterns of (a)  $\text{Li}/\text{Al} = 1$ ,  $T = 20^\circ\text{C}$ , (b)  $\text{Li}/\text{Al} = 1$ ,  $T = 40^\circ\text{C}$ , (c)  $\text{Li}/\text{Al} = 0.6$ ,  $T = 60^\circ\text{C}$ , (d)  $\text{Li}/\text{Al} = 1.7$ ,  $T = 60^\circ\text{C}$ , (e)  $\text{Li}/\text{Al} = 0.9$ ,  $T = 60^\circ\text{C}$  and (f)  $\text{Li}/\text{Al} = 1.1$ ,  $T = 60^\circ\text{C}$ .

In Figure 1, the XRD images with  $\text{Li}/\text{Al} = 0.9$ – $1.1$  are basically the same in terms of the intensity, but differ in microstructure. As shown in Figure 2e,f, it can be seen that the molecular sieve from the crystallization of the geopolymer was at the nanoscale, while the Li-ABW molecular sieve prepared through hydrothermal reaction was mostly at the micrometer scale [27–32]. It has been proven that, under the appropriate conditions, the geopolymerization reaction will produce microcrystals that are favorable for zeolite formation. Overlapped zeolite crystals can also be observed, which are common in reports of geopolymer conversion [32–34]. In terms of stacking, the microstructure of  $\text{Li}/\text{Al} = 0.9$  with a relatively small amount of activator is relatively dense, and  $\text{Li}/\text{Al} = 1.1$  is the opposite, but has the accumulation of a larger single crystal caused by the high alkalinity in the morphology. It is possible that more activators lead to an increase in the amount of gel, which are essential precursors for molecular sieves, and that the corresponding amount of  $\text{Li}^+$  content may lead to an improved induction of zeolite formation.

### 2.3. In-Situ Infrared Spectroscopy Analysis

In order to further explore the conversion mechanism of the lithium geopolymer, the slurry was analyzed using in-situ infrared spectroscopy. Figure 3b shows the in-situ infrared image of  $\text{Li}/\text{Al} = 1.1$  and  $T = 60^\circ\text{C}$  when the reaction time is 0–360 min. Using the same recording method as in Figure 3b, f shows the image of  $\text{Li}/\text{Al} = 0.6$ . As the curve displacement of the equipment led to its absorption peak strength rising slowly with the passage of time (which can be seen from Figure 3c), the curve was made independent and was analyzed in the experiment. For the geopolymer, the fingerprint area of  $800$ – $1200\text{ cm}^{-1}$  is more significant. In addition, there are many vibration modes of Si–O–Si in the raw



materials (including asymmetric stretching vibration, symmetric stretching vibration, and bending vibration) within  $370\text{--}1300\text{ cm}^{-1}$  [35]. In conclusion, combined with the instrument parameters, the measuring range was  $650\text{--}1200\text{ cm}^{-1}$ . It can be seen from Figure 3a,b that the absorption peak first appeared at  $1069\text{ cm}^{-1}$  in 0–5 min, shifted to  $1078\text{ cm}^{-1}$  in 30 min, and then gradually disappeared and merged into the strong  $1094\text{ cm}^{-1}$ . The vanishment of  $1069\text{ cm}^{-1}$  is considered to be the dissolution of the Si–O–Si bond in the MK under the action of alkali [36].

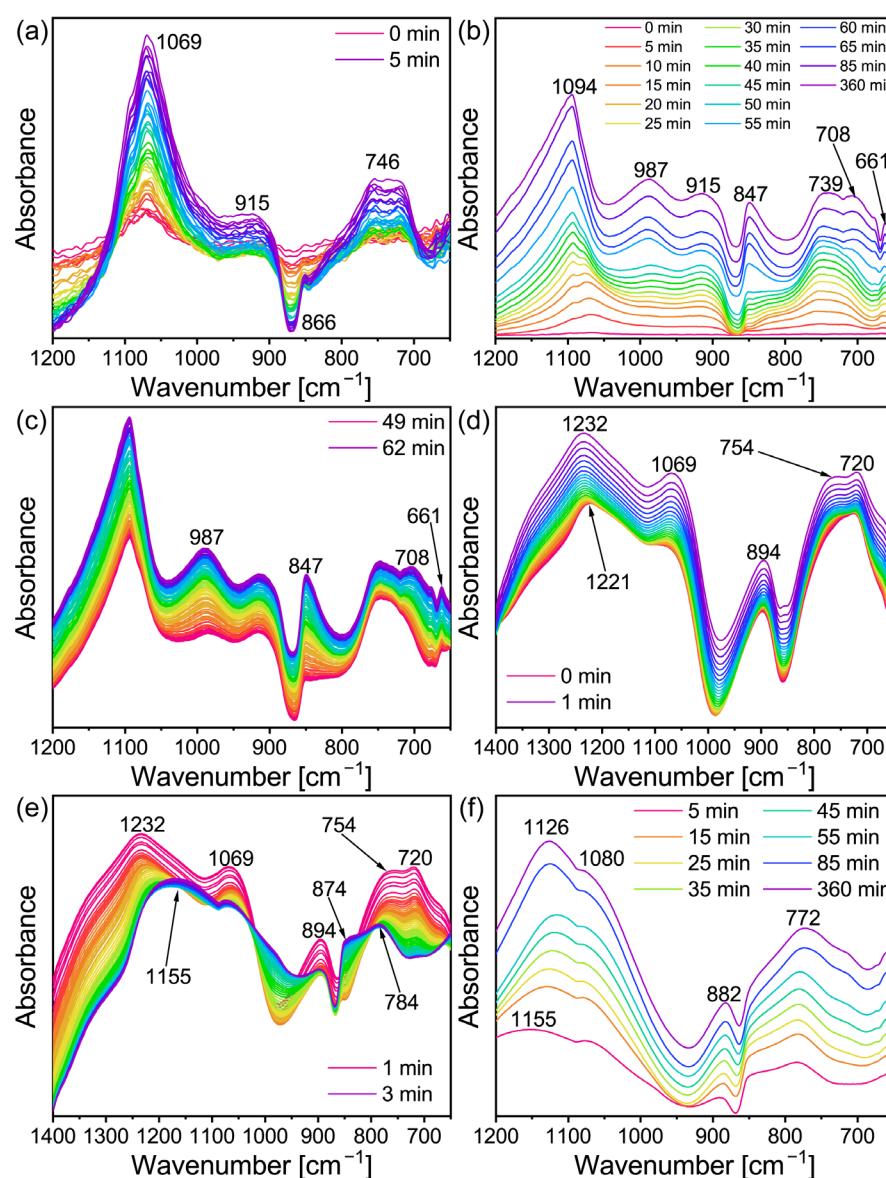


**Figure 3.** In situ DRIFTS of (a) Li/Al = 1.1,  $t = 0\text{--}5$  min (b) Li/Al = 1.1,  $t = 0\text{--}360$  min, (c) Li/Al = 1.1,  $t = 49\text{--}62$  min, (d) Li/Al = 0.6,  $t = 0\text{--}1$  min (e) Li/Al = 0.6,  $t = 1\text{--}3$  min and (f) Li/Al = 0.6,  $t = 5\text{--}360$  min.

The aluminum in the Al–O bond in the MK is bonded with the six-coordination, while in the Al–O tetrahedron, it formed after alkali excitation in the four-coordination, and  $[\text{AlO}_4]$  occupies the original  $[\text{SiO}_4]$  after polycondensation, which leads to the change in the chemical environment of Si and Al [37]. For the Na-activated MK, the absorption peak of the stretching vibration of the Si–O–T (T = Al or Si) bond generally appears at  $1076\text{ cm}^{-1}$  [37,38], however, it may shift due to the use of lithium hydroxide as the activator. In general, the peak at  $1095\text{ cm}^{-1}$  corresponds to the asymmetric vibration of the Si–O bond. In addition, the absorption peak of the aluminum-rich phase Q3 at the initial reaction stage

corresponds to  $1093\text{ cm}^{-1}$  [35]. Therefore, the strong peak at  $1094\text{ cm}^{-1}$  may be the result of the joint contribution of the above three factors. The absorption peak at  $746\text{ cm}^{-1}$  may be the joint action of the stretching vibration of the Al-O bond [39] and the symmetric stretching vibration of Si-O-T, which generally occurs between  $600\text{--}800\text{ cm}^{-1}$  [35]. The increase in the intensity of the absorption peak here confirmed the dissolution of the six-coordinate Al in the geopolymerization reaction. The peak that appeared at  $915\text{ cm}^{-1}$  might correspond to the asymmetric expansion of the Si-O-T bond, which is active in the geopolymeric reaction [35]. The generation of zeolite led this toward the high wavenumber. However, the infrared spectrum changed with time.

There were obvious changes in the in-situ infrared image after approximately 50–60 min, as can be seen in Figure 3b. As shown in Figure 3c, the 49–62 min ATR-FT-IR image was separated. There are obvious adsorption peaks at  $987\text{ cm}^{-1}$ ,  $847\text{ cm}^{-1}$ ,  $708\text{ cm}^{-1}$ , and  $661\text{ cm}^{-1}$ , and there is no sharp change when the reaction lasts for 360 min (the top curve in Figure 3b). On one hand, the geopolymer slurry is actually solidified during the induction period of zeolite formation [40], which means that the transformation may occur during curing if the relevant conditions are suitable. On the other hand, these peaks appeared almost simultaneously. This indicated that the geopolymer may have been transformed at this time point. In addition, Figure 4 can also prove this inference, even if the intensity of the characteristic peak is low. At the beginning of the reaction, a relatively excessive amount of lithium hydroxide monohydrate (JPCDS card No. 01-075-0883) was detected in the sample, which also proved that the low-temperature cryogenic method of liquid nitrogen can suspend the geopolymerization reaction at the corresponding time point. As can be seen in the figure, with the progress of the geopolymerization reaction, the lithium hydroxide monohydrate continues to dissolve, its characteristic peak gradually disappears, and the entire system transforms into an amorphous geological polymer. The characteristic peak of the Li-ABW-type molecular sieve appears until the reaction proceeds to 55 min. It can be seen from this that, under the conditions of this experiment, when the reaction time is more than 55 min, the crystallization of the zeolite is actually carried out synchronously with the solidification and curing of the geopolymer. Moreover, the absorption peak at  $746\text{ cm}^{-1}$  shifts towards the low wave number during the reaction; this could be interpreted as a change in the bond length and angle of the Si-O-Si in the gel [41].

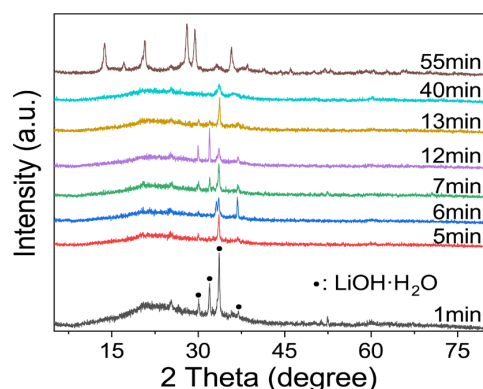


**Figure 4.** XRD characterization of Li/Al = 1.1 with different curing time.

In contrast to the transformation group, the change in the absorption peak in the geopolymer group was mainly concentrated in the 1–3 min period. In the case of the rising relative intensity displacement between the curves (Figure 3c), the absorption peak in Figure 3e shows strength weakening. This means that the corresponding raw material was involved in the reaction and was consumed. In addition, the peak shifted and weakened due to the reduction in other vibration contributions, and the relevant absorption peak may be a part of the original synthetic broad peak. There are two aspects that can support this point: Firstly, the shift from  $1069\text{ cm}^{-1}$  to  $1080\text{ cm}^{-1}$ , which might be due to the joint contribution of the Al dissolution to increase the signal of the asymmetric stretching of the

Al-O bond at  $1085\text{ cm}^{-1}$  [35] and the consumption of MK in the reaction process. Lastly, two absorption peaks ( $720\text{ cm}^{-1}$  and  $754\text{ cm}^{-1}$ ) corresponded to the disappearance of the MK. A new peak was separated at  $784\text{ cm}^{-1}$ , which may be the symmetric stretching vibration of Si-O-T [38].

Figure 3f shows that the absorption peak of the geopolymer sample with  $\text{Li}/\text{Al} = 0.6$  changed little with time and only partially shifted, which also proved that the new peaks in Figure 3b represented the formation of a lithium molecular sieve. The absorption peak that finally shifted at  $1126\text{ cm}^{-1}$  requires further discussion; it shifted from  $1221\text{ cm}^{-1}$  at the beginning of the reaction to  $1232\text{ cm}^{-1}$ , then shifted to  $1116\text{ cm}^{-1}$  as the reaction proceeded, and ultimately returned to  $1126\text{ cm}^{-1}$ . The reason for the first shift to the high wavenumber is the stretching vibration of the Al-O band [39]. The absorption peak at  $1221\text{ cm}^{-1}$  may correspond to the stretching vibration of the Si-O-Si bond of Q0 [35] as the  $\text{Si}/\text{Al}$  of MK is close to one, Si and Al were dissolved at the same time in the initial reaction, and the gel was relatively rich in silicon; therefore, the main peak will shift to the high wavenumber [42]. The subsequent situation, from high to low then to high, might be due to the relatively faster dissolution of aluminum in the MK during the geopolymerization process, which generates more aluminosilicates, causing the main peak of Si-O-T to shift to a low wavenumber. As the reaction progressed, further silicon dissolution improves the degree of cross-linking, which causes the main peak to shift back [42]. This is further supported by the work of A. et al. [43], who used sodium hydroxide to activate F-type fly ash and proved that Al-rich gel was first generated at the initial stage of the activation. The silicon source was gradually dissolved and the gel was transformed into a silicon-rich phase with the extension of the curing time.

The in-situ infrared image of the lithium-based geopolymer under high alkali conditions ( $\text{Li}/\text{Al} = 1.7$ ) is shown in Figure 5a,b. It can be seen that in the case of an excessive addition of lithium hydroxide monohydrate, the image at the initial stage of the geopolymerization reaction is significantly different from those in Figure 3a,d. Firstly, the absorption peak at  $1040\text{ cm}^{-1}$  may be caused by the Si-O-Si stretching vibration of unreacted metakaolin [44–46]. It then shifts to a low wavenumber, of  $1003\text{ cm}^{-1}$ , which may be related to the superposition of the asymmetric stretching peaks representing the Si-O-T ( $\text{T} = \text{Si}, \text{Al}$ ) bond at  $986\text{ cm}^{-1}$  and  $993\text{ cm}^{-1}$ , as well as the asymmetric stretching peaks [47] of the Si-O-T ( $\text{T} = \text{Si}, \text{Al}$ ) bond of Q2 generated at the initial stage of the reaction. Secondly, the absorption peak appears at  $870\text{ cm}^{-1}$  may represent the end vibration of Si-O [48], which is reflected in both  $\text{Li}/\text{Al} = 0.6$  and  $1.1$ , which is also an example of the absence of zeolite formation. In addition to the absorption peak mentioned above, the absorption peak at  $857\text{ cm}^{-1}$ , which occurs later than  $870\text{ cm}^{-1}$ , may be related to the asymmetric stretching vibration of the Si-O bond. Finally, the absorption peak appearing at  $673\text{ cm}^{-1}$  may be related to the Si-O-T ( $\text{T} = \text{Si}, \text{Al}$ ) [49] and the vibration of the O-Si-O bond. The decrease in the intensity at  $740\text{ cm}^{-1}$  may be caused by the complete dissolution of metakaolin in the presence of excessive sodium lithium hydroxide addition.

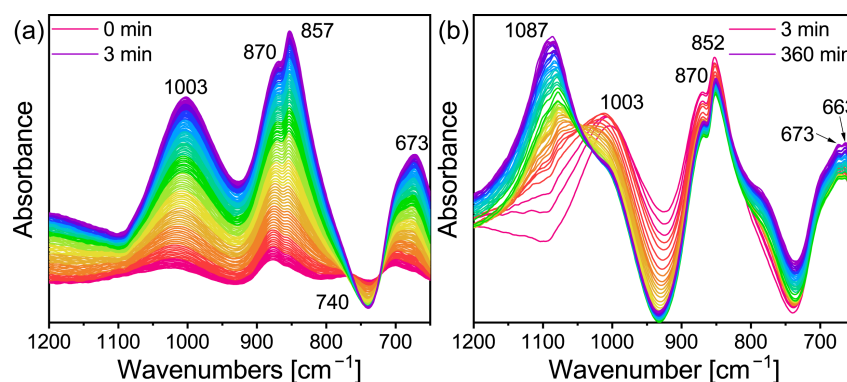


**Figure 5.** In situ DRIFTS of (a)  $\text{Li}/\text{Al} = 1.7$ ,  $t = 0\text{--}3\text{ min}$  (b)  $\text{Li}/\text{Al} = 1.1$ ,  $t = 3\text{--}360\text{ min}$ .

As the reaction continues, as shown in Figure 5b, the absorption peaks at  $870\text{ cm}^{-1}$ ,  $852\text{ cm}^{-1}$ , and  $673\text{ cm}^{-1}$  that appear in Figure 5a do not change significantly. The changes in the image are as follows: First, the main peak at  $1003\text{ cm}^{-1}$  shifted and the intensity decreased, and finally it shifted to  $1087\text{ cm}^{-1}$  at the end of the reaction. Similarly to the cause of the shift of the main peak in Figure 3b, when the amount of lithium hydroxide is sufficient, the absorption peak corresponding to the asymmetric stretching vibration of the Si-O-T bond at  $1076\text{ cm}^{-1}$  [48], the asymmetric contraction of the Al-O bond at  $1085\text{ cm}^{-1}$  with the dissolution of aluminum, the asymmetric stretching vibration of the Si-O bond at  $1095\text{ cm}^{-1}$ , the absorption peak of the aluminum-rich phase Q3 appearing at  $1093\text{ cm}^{-1}$  [35], and the chemical environment of Si and Al change [37]. Factors such as the vibration of Si-O [50] and the presence of Q3 bonds [51] jointly lead to the occurrence of an absorption peak at  $1087\text{ cm}^{-1}$ . The difference is that, due to the absence of zeolite formation, there is no blocking effect on the surface of the geopolymer, resulting in the detection of the signal of the asymmetric stretching peak [47] of the Si-O-T of Q2 in the geopolymer; therefore, the absorption peak at  $1003\text{ cm}^{-1}$  remains in the image. In addition, the occurrence time of the absorption peak at  $663\text{ cm}^{-1}$  is similar to that at  $661\text{ cm}^{-1}$  in  $\text{Li}/\text{Al} = 1.1$ , which may be related to the crystal plane corresponding to the characteristic peak of  $35.81^\circ$  in the XRD image in Figure 1a.

In summary, the following conclusion has been proposed: On one hand, the conversion time of lithium-based geopolymers is about 50 min from the beginning of the geopolymerization, which to some extent supports the theory that the conversion time of in-situ zeolite may be earlier than the solidification time of the geopolymer. On the other hand, the low alkali system shows the consistency of the in-situ infrared curve, and the complexity of the changes are most active at 1–3 min. In contrast, the transformation group and the high-alkali system show good inducibility at the initial stage of the reaction, which may be related to the inductive effect of zeolite microcrystals on the gel of the geopolymers.

#### 2.4. XPS Analysis

To further determine the formation mechanism of lithium zeolite, as shown in Figures 6 and 7, the elemental composition of the initial sample (reaction time: 1 min), the pre-conversion sample (40 min), the initial conversion sample (55 min), and the completely converted sample (reaction time: 96 h) were detected using XPS.

According to a previous report [27,52], there are usually four chemical forms of samples in geological polymers and zeolites. Therefore, when performing peak fitting on the O 1s high-resolution spectrum, Si-OH, Si-O-Al, Si-O-Si, and Si-O-Li are selected. From the beginning of the reaction until the conversion of the geopolymer, the electron binding energy decreased, with Al decreasing from 74.25 eV to 73.78 eV, while Si decreased from 101.88 eV to 101.58 eV, which may be due to the increase in the release of Si and Al elements from the metakaolin, indicating that geopolymerization is mainly carried out.

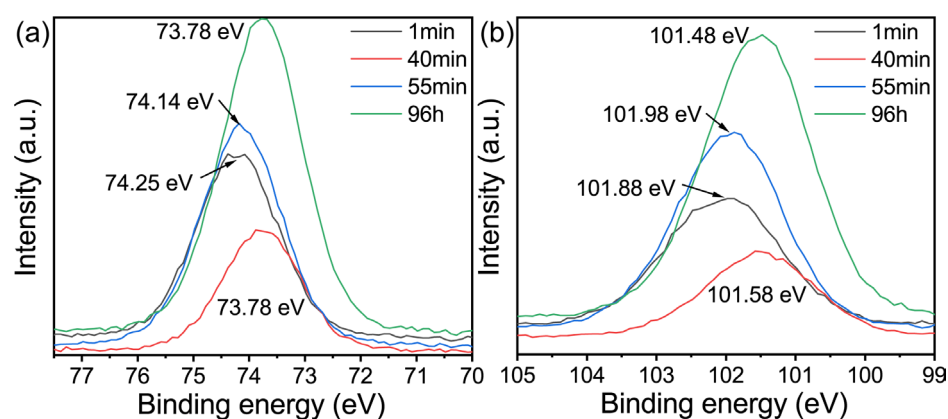
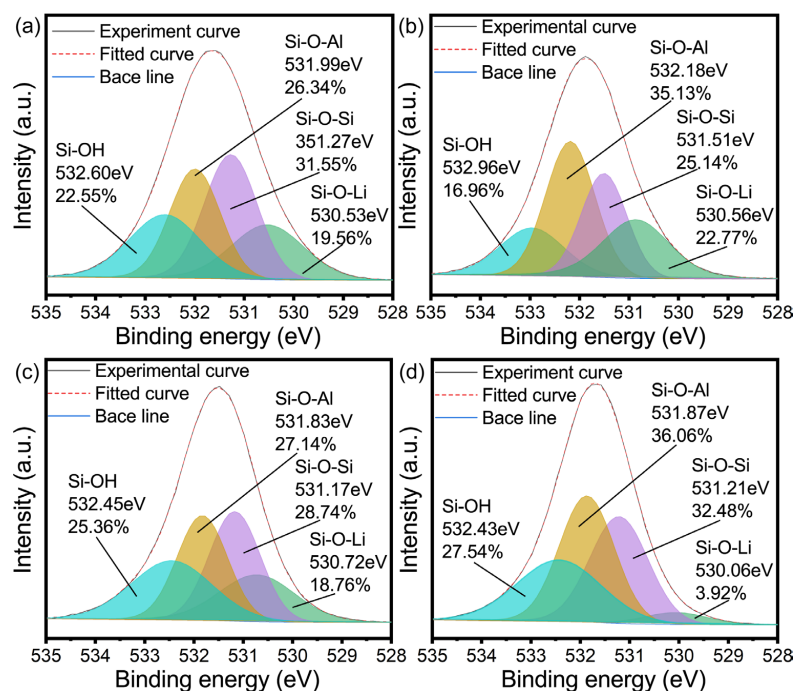


Figure 6. High resolution XPS spectra of (a) Al (2p), (b) Si (2p).





**Figure 7.** O 1s high resolution XPS spectra of (a) 1 min, (b) 40 min, (c) 55 min and (d) 96 h.

With the increase in the curing time, the electronic binding energy of Al and Si increases at the initial stage of zeolite conversion, which may be because the lithium-based geopolymer reaction system needs to go through a process from disorder to order during crystallization, one of which involves the lithium entering into the geopolymer gel structure, which will enter into the zeolite skeleton in the form of a lithium ion during the process of geopolymer crystallization into zeolite. Combining this with Figure 7c,d, it can be seen that the content of Li-O-Si decreases sharply during the transformation of the lithium-based geopolymer. On the other hand, the geopolymer gel should rearrange the microcrystals generated in the geopolymerization as the crystal nucleus to produce Si/Al close to one and to generate zeolite. Both of the above may contribute to the increase in the electron binding energy of Al and Si. At the same time, the increase in the electron binding energy before and after transformation also reflects the fact that the change of the geopolymer gel system is different from the formation of geopolymer gel, which to some extent proves the formation of the boiling stone phase in this process. With the increase in the crystallization degree, the total energy of the system decreases. At this time, Al and Si exist in the form of a zeolite skeleton. In this case, compared with the geopolymer gel, its chemical environment is more stable. Therefore, the electronic binding energy of Al and Si decreases continuously during the reaction process and is ultimately less than the electronic binding energy of Al and Si in the initial reaction of the geopolymer.

From the peak fitting of the high-resolution spectrum of O 1s, as shown in Figure 7, the following inference can be drawn: Firstly, it can be seen that the content of Si-O-Al significantly increased from the beginning of the reaction to the beginning of crystallization, which may be due to the relatively faster dissolution rate of Al in the early stage of the geopolymerization reaction. Secondly, Figure 7b,c show that the changes in the content of the Si-O-Al and Si-O-Si bonds before and after the formation of zeolite. With the dissolution of more Si, and under the control of the main crystal form  $\text{Li}_4\text{Al}_4\text{Si}_4\text{O}_{16} \cdot 4\text{H}_2\text{O}$  (this can be seen from XRD images), the content of these two bonds tends to be consistent. Finally, it can be seen from Figure 7d that after deducting the content of Si-O-Li corresponding to Si-O-Al in the gel, the content of the Si-O-Si and Si-O-Al bonds is almost the same, which also explains the contribution of the zeolite transformation in Figure 7c to the convergence of the content of the Si-O-Si and Si-O-Al bonds.

Geopolymerization generally reduces the energy of the system, while the crystallization process itself increases the energy of the system. However, after complete crystallization, the overall energy is lower than that of the system in the state of the geopolymer, which to some extent proves that the geopolymer is a good precursor for zeolite conversion. The crystallization process of the geopolymer-based zeolite is accompanied by the process of Li separating from the L-A-S-H gel and entering the zeolite skeleton. In other words, in the process of geopolymer conversion, the rearrangement of the Si and Al gel and the separation of Li belong to two steps, respectively, and are not directly converted with L-A-S-H as the raw material.

### 2.5. TG-DTG Analysis

Figure 8 shows the TG-DTG curves of the samples with reaction times of 1 min, 40 min, 55 min, and 96 h. According to the figure, there are three weight loss intervals for the geological polymer samples: 25–200 °C, 200–500 °C, and 600–800 °C, which correspond to the mass loss peak of the geopolymer gel L-A-S-H, hydrotalcite [53], a mass loss peak in which the lithium hydroxide monohydrate loses crystalline water and decomposes, and a mass loss peak in lithium carbonate, respectively. The weight loss range of the molecular sieve samples mainly occurs at 100–300 °C, and the corresponding crystal form of the molecular sieve collapses from  $\text{Li}_4\text{Al}_4\text{Si}_4\text{O}_{16} \cdot 4\text{H}_2\text{O}$  to  $\text{Li}_2\text{Al}_2\text{Si}_2\text{O}_8 \cdot 0.18\text{H}_2\text{O}$  after water loss. It can be seen that the formation of zeolite has significantly changed the properties of the lithium-based geopolymer: First, in general, the zeolite generated in situ by the geopolymer usually grows on the surface of the geopolymer gel, and the zeolite generated in situ completely seals the L-A-S-H gel to keep it unchanged in the weight loss temperature range of the unconverted lithium-based geopolymer. Secondly, the formation of zeolite induced the formation of geopolymer gel to a certain extent, making the original weight loss segment of the hydrotalcite disappear. Finally, the addition of lithium hydroxide monohydrate is relatively excessive, while the conversion group has no significant changes in the corresponding dehydration and decomposition stages of the lithium hydroxide monohydrate, which may also be related to the fixation of the zeolite on the alkali.

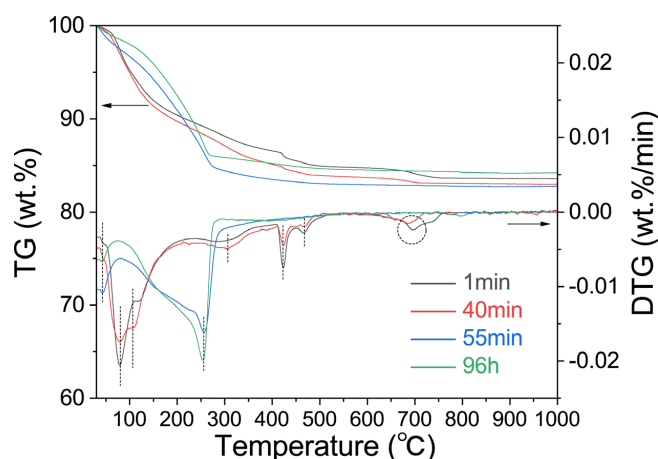


**Figure 8.** TG-DTG characterization of Li/Al = 1.1 with different curing time.

The formation of geopolymer-based lithium zeolite will have an impact on the geopolymer system. The transformation of the zeolite on the surface of the geopolymer will seal the L-A-S-H gel, as well as the excess alkali in the gel pore solution or system, which will fix the excess alkali later.

### 3. Conclusions

In this paper, Li-ABW zeolite was prepared in situ under non-hydrothermal conditions. The results showed that the optimum Si/Al ratio formed by a molecular sieve is 1.1. The geopolymer can be transformed at 30 °C, and the optimal temperature is about 60 °C. The

formation of zeolite was characterized using in-situ infrared spectroscopy. The in-situ crystallization took place approximately 50 min after the reaction under the above optimal conditions. This work characterized the induction of zeolite microcrystals on a geopolymer gel, characterized the process of the in-situ transformation of zeolite using a geopolymer, and proved that geopolymer can be used as a good precursor of zeolite. In summary, this experiment provides a simple process for the preparation of lithium zeolite with lower energy consumption, which might be applied as a solid electrolyte.

#### 4. Materials and Methods

##### 4.1. Materials

SiO<sub>2</sub> (51.02 wt.%), Al<sub>2</sub>O<sub>3</sub> (44.99 wt.%), etc. (3.99 wt.%) in metakaolin were provided by Inner Mongolia Super New Material Co., Ltd Inner Mongolia, Hohhot, China. Lithium hydroxide monohydrate (AR) was purchased from Shanghai Aladdin Biochemical Technology Co. (Shanghai, China) Deionized water was provided by the School of Chemistry and Chemical Engineering, Guangxi University.

##### 4.2. Characterization of the Samples

The synthesis steps of the Li/Al = 1 geopolymer-based lithium molecular sieve are as follows: 100 g metakaolin was mixed with 37.68 g LiOH·H<sub>2</sub>O and added to a certain amount of deionized water (due to the low solubility of LiOH, the study of H<sub>2</sub>O/Li<sub>2</sub>O lost its significance. In this experiment, the slurry capable of forming a geopolymer was used as the adding standard of water quantity, which was approximately consistent with the quality of metakaolin used), then the mixture was stirred evenly with dispersant. The slurry was cast into a disk mold and cured at 60 °C for 24 h. After demolding, the geopolymer-based Li-ABW was obtained. Other samples were prepared in the same manner as described above, changing the curing temperature, time, and Li/Al ratio. Most samples used for testing are freeze-dried, the samples at the corresponding time point (accurate to the minute) underwent cryogenic treatment with liquid nitrogen and were then freeze-dried.

##### 4.3. Synthesis of the Zeolites

The X-ray diffraction (XRD) characterization of the samples was performed with Rigaku MiniFlex 600 (Tokyo, Japan) using Ni filters and Cu (K $\alpha$ ) radiation ( $\lambda = 1.392 \text{ \AA}$ ) at a voltage of 40 kV and current of 15 mA. The scanning range( $2\theta$ ) was between 5 and 80°, under the conditions of 0.02° step size, 0.5 s dwell time, and 5°/min scanning rate. The morphology of the geopolymer gel and zeolite was photographed using a field emission scanning electron microscope (FE-SEM) (Hitachi, SU8220, Tokyo, Japan) after gold sputtering. In-situ diffuse reflectance infrared Fourier transform spectroscopy (DRIFTS) in the range of 650~4000 cm<sup>-1</sup> of the samples in an in-situ cell was recorded with a spectrometer (Thermo Fisher Scientific (Waltham, MA, USA) IS50. X-ray photoelectron spectrometer (XPS) characterization of the samples was performed with Thermo Scientific Nexsa. TG/TGA characterization of the samples was performed with a TGA2 thermogravimetric analyzer.

**Author Contributions:** Conceptualization, Q.Y. and X.C.; methodology, Y.H.; writing—review and editing, H.D. All authors have read and agreed to the published version of the manuscript.

**Funding:** This work was supported by the Chinese Natural Science Fund (Grant: 51772055) and the Guangxi Natural Science Fund (grant: 2022GXNSFDA035062).

**Institutional Review Board Statement:** Not applicable.

**Informed Consent Statement:** Not applicable.

**Data Availability Statement:** Not applicable.

**Conflicts of Interest:** The authors declare no conflict of interest.

## References

- Manthiram, A.; Yu, X.; Wang, S. Lithium battery chemistries enabled by solid-state electrolytes. *Nat. Rev. Mater.* **2017**, *2*, 16103. [\[CrossRef\]](#)
- Wang, Y.; Hoang, B.; Hoerauf, J.; Lee, C.; Lin, C.F.; Rubloff, G.W.; Lee, S.B.; Kozen, A.C. Hot and Cold Pressed LGPS Solid Electrolytes. *J. Electrochem. Soc.* **2021**, *168*, 010533. [\[CrossRef\]](#)
- Liu, T.; Zhang, X.; Wang, X.; Yu, J.; Li, L. A review of zirconia-based solid electrolytes. *Ionics* **2016**, *22*, 2249–2262. [\[CrossRef\]](#)
- Porz, L.; Swamy, T.; Sheldon, B.W.; Rettenwander, D.; Frömling, T.; Thaman, H.L.; Berendts, S.; Uecker, R.; Carter, W.C.; Chiang, Y.-M. Mechanism of Lithium Metal Penetration through Inorganic Solid Electrolytes. *Adv. Energy Mater.* **2017**, *7*, 1701003. [\[CrossRef\]](#)
- Yang, Y.; Li, W.; Xu, X.; Tong, G. Heat dissipation analysis of different flow path for parallel liquid cooling battery thermal management system. *Int. J. Energy Res.* **2020**, *44*, 5165–5176. [\[CrossRef\]](#)
- Xi, S.; Zhao, Q.; Chang, L.; Huang, X.; Cai, Z. The dynamic failure mechanism of a lithium-ion battery at different impact velocity. *Eng. Fail. Anal.* **2020**, *116*, 104747. [\[CrossRef\]](#)
- Li, Y.; Wei, C.; Sheng, Y.; Jiao, F.; Wu, K. Swelling Force in Lithium-Ion Power Batteries. *Ind. Eng. Chem. Res.* **2020**, *59*, 12313–12318. [\[CrossRef\]](#)
- Or, T.; Gourley, S.W.; Kaliyappan, K.; Yu, A.; Chen, Z. Recycling of mixed cathode lithium-ion batteries for electric vehicles: Current status and future outlook. *Carbon Energy* **2020**, *2*, 6–43. [\[CrossRef\]](#)
- Chi, X.; Li, M.; Di, J.; Bai, P.; Song, L.; Wang, X.; Li, F.; Liang, S.; Xu, J.; Yu, J. A highly stable and flexible zeolite electrolyte solid-state Li-air battery. *Nature* **2021**, *592*, 551–557. [\[CrossRef\]](#)
- Zhang, P.; Chen, X.; Leng, Y.; Dong, Y.; Jiang, P.; Fan, M. Biodiesel production from palm oil and methanol via zeolite derived catalyst as a phase boundary catalyst: An optimization study by using response surface methodology. *Fuel* **2020**, *272*, 117680. [\[CrossRef\]](#)
- Wang, M.-Y.; Han, S.-H.; Chao, Z.-S.; Li, S.-Y.; Tan, B.; Lai, J.-X.; Guo, Z.-Y.; Wei, X.-L.; Jin, H.-G.; Luo, W.-B.; et al. Celgard-supported LiX zeolite membrane as ion-permselective separator in lithium sulfur battery. *J. Membr. Sci.* **2020**, *611*, 118386. [\[CrossRef\]](#)
- Ding, Z.; Tang, Q.; Liu, Y.; Yao, P.; Liu, C.; Liu, X.; Wu, J.; Lavorgna, M. Integrate multifunctional ionic sieve lithiated X zeolite-ionic liquid electrolyte for solid-state lithium metal batteries with ultralong lifespan. *Chem. Eng. J.* **2022**, *433*, 133522. [\[CrossRef\]](#)
- Xu, J.; Xiao, X.; Zeng, S.; Cai, M.; Verbrugge, M.W. Multifunctional Lithium-Ion-Exchanged Zeolite-Coated Separator for Lithium-Ion Batteries. *ACS Appl. Energy Mater.* **2018**, *1*, 7237–7243. [\[CrossRef\]](#)
- Davidovits, J. Geopolymer and geopolymeric materials. *J. Therm. Anal.* **1989**, *35*, 429–441. [\[CrossRef\]](#)
- Davidovits, J. GEOPOLYMERS: Man-Made Rock Geosynthesis and the Resulting Development of Very Early High Strength Cement. *J. Mater. Educ.* **1994**, *16*, 91–139.
- Duxson, P.; Fernández-Jiménez, A.; Provis, J.L.; Lukey, G.C.; Palomo, A.; van Deventer, J.S. Geopolymer technology: The current state of the art. *J. Mater. Sci.* **2007**, *42*, 2917–2933. [\[CrossRef\]](#)
- Van Deventer, J.S.J.; Provis, J.L.; Duxson, P.; Lukey, G.C. Reaction mechanisms in the geopolymeric conversion of inorganic waste to useful products. *J. Hazard. Mater.* **2007**, *139*, 506–513. [\[CrossRef\]](#)
- Rožek, P.; Król, M.; Mozgawa, W. Geopolymer-zeolite composites: A review. *J. Clean. Prod.* **2019**, *230*, 557–579. [\[CrossRef\]](#)
- Tang, Q.; He, Y.; Wang, Y.P.; Wang, K.T.; Cui, X.M. Study on synthesis and characterization of ZSM-20 zeolites from metakaolin-based geopolymers. *Appl. Clay Sci.* **2016**, *129*, 102–107. [\[CrossRef\]](#)
- Han, L.; Wang, X.; Wu, B.; Zhu, S.; Wang, J.; Zhang, Y. In-situ synthesis of zeolite X in foam geopolymer as a CO<sub>2</sub> adsorbent. *J. Clean. Prod.* **2022**, *372*, 133591. [\[CrossRef\]](#)
- Zheng, Z.; Ma, X.; Zhang, Z.; Li, Y. In-situ transition of amorphous gels to Na-P1 zeolite in geopolymer: Mechanical and adsorption properties. *Constr. Build. Mater.* **2019**, *202*, 851–860. [\[CrossRef\]](#)
- Ye, Q.; Su, Q.; Deng, L.; Wan, H.; He, Y.; Cui, X. Self-assembled geopolymer-based microspheres supported nanoclusters for CO<sub>2</sub> hydrogenation. *J. CO<sub>2</sub> Util.* **2022**, *55*, 101820. [\[CrossRef\]](#)
- Guan, L.; Wang, Z.; Lu, D. Evolution of Zeolite Crystals in Self-Supporting Faujasite Blocks: Effects of Hydrothermal Conditions. *Materials* **2019**, *12*, 1965. [\[CrossRef\]](#) [\[PubMed\]](#)
- Wei, E.; Wang, K.; Muhammad, Y.; Chen, S.; Dong, D.; Wei, Y.; Fujita, T. Preparation and conversion mechanism of different geopolymer-based zeolite microspheres and their adsorption properties for Pb<sup>2+</sup>. *Sep. Purif. Technol.* **2022**, *282*, 119971. [\[CrossRef\]](#)
- Xuemin, C.; Yan, H.; Leping, L.; Jinyu, C. NaA zeolite synthesis from geopolymer precursor. *MRS Commun.* **2011**, *1*, 49–51. [\[CrossRef\]](#)
- Xu, M.X.; He, Y.; Wang, Y.P.; Cui, X.M. Preparation of a non-hydrothermal NaA zeolite membrane and defect elimination by vacuum-inhalation repair method. *Chem. Eng. Sci.* **2017**, *158*, 117–123. [\[CrossRef\]](#)
- He, P.Y.; Zhang, Y.J.; Chen, H.; Han, Z.C.; Liu, L.C. Low-cost and facile synthesis of geopolymer-zeolite composite membrane for chromium (VI) separation from aqueous solution. *J. Hazard. Mater.* **2020**, *392*, 122359. [\[CrossRef\]](#)
- Yao, Z.; Ye, Y.; Xia, M. Synthesis and Characterization of Lithium Zeolites with ABW Type from Coal Fly Ash. *Environ. Prog. Sustain. Energy* **2012**, *32*, 790–796. [\[CrossRef\]](#)
- Yao, Z.T.; Xia, M.S.; Ye, Y.; Zhang, L. Synthesis of zeolite Li-ABW from fly ash by fusion method. *J. Hazard. Mater.* **2009**, *170*, 639–644. [\[CrossRef\]](#)



30. He, P.; Zhang, Y.; Zhang, X.; Chen, H. Diverse zeolites derived from a circulating fluidized bed fly ash based geopolymer for the adsorption of lead ions from wastewater. *J. Clean. Prod.* **2021**, *312*, 127769. [\[CrossRef\]](#)
31. Li, C.J.; Zhang, Y.J.; Chen, H.; He, P.Y.; Zhang, Y.; Meng, Q. Synthesis of fly ash cenospheres-based hollow ABW zeolite for dye removal via the coupling of adsorption and photocatalysis. *Adv. Powder Technol.* **2021**, *32*, 3436–3446. [\[CrossRef\]](#)
32. Wang, K.; Wang, F.; Chen, F.; Cui, X.; Wei, Y.; Shao, L.; Yu, M. One-Pot Preparation of NaA Zeolite Microspheres for Highly Selective and Continuous Removal of Sr(II) from Aqueous Solution. *ACS Sustain. Chem. Eng.* **2019**, *7*, 2459–2470. [\[CrossRef\]](#)
33. Wang, H.; Yan, C.; Li, D.; Zhou, F.; Liu, Y.; Zhou, C.; Komarneni, S. In situ transformation of geopolymer gels to self-supporting NaX zeolite monoliths with excellent compressive strength. *Microporous Mesoporous Mater.* **2018**, *261*, 164–169. [\[CrossRef\]](#)
34. Hu, G.; Rohani, S.; Jiang, X.; Li, J.; Liu, Q.; Liu, W. CO<sub>2</sub> Mineral Sequestration and Faujasite Zeolite Synthesis by Using Blast Furnace Slag: Process Optimization and CO<sub>2</sub> Net-Emission Reduction Evaluation. *ACS Sustain. Chem. Eng.* **2021**, *9*, 13963–13971. [\[CrossRef\]](#)
35. Revathi, T.; Jeyalakshmi, R. Fly ash-GGBS geopolymer in boron environment A study on rheology and microstructure by ATR FT-IR and MAS NMR. *Constr. Build. Mater.* **2021**, *267*, 120965. [\[CrossRef\]](#)
36. Król, M.; Rožek, P.; Chlebda, D.; Mozgawa, W. ATR/FT-IR studies of zeolite formation during alkali-activation of metakaolin. *Solid State Sci.* **2019**, *94*, 114–119. [\[CrossRef\]](#)
37. Zhang, C.; Wang, X.; Hu, Z.; Wu, Q.; Zhu, H.; Lu, J. Long-term performance of silane coupling agent/metakaolin based geopolymer. *J. Build. Eng.* **2021**, *36*, 102091. [\[CrossRef\]](#)
38. Adjdir, M.; Ali-Dahmane, T.; Weidler, P.G. The structural comparison between Al-MCM-41 and B-MCM-41. *C. R. Chim.* **2009**, *12*, 793–800. [\[CrossRef\]](#)
39. Watling, H. Spectroscopy of Concentrated Sodium Aluminate Solutions. *Appl. Spectrosc.* **1998**, *52*, 250–258. [\[CrossRef\]](#)
40. Lee, W.K.W.; Van Deventer, J.S.J. The Effect of Ionic Contaminants on the Early Age Properties of Alkali-Activated Fly Ash Based Cements. *Cem. Concr. Res.* **2022**, *32*, 577–584. [\[CrossRef\]](#)
41. Innocenzi, P. Infrared spectroscopy of sol-gel derived silica-based films: A spectra-microstructure overview. *Langmuir* **2007**, *23*, 9076–9082. [\[CrossRef\]](#)
42. Hajimohammadi, A.; Provis, J.L.; Van Deventer, J.S. Effect of Alumina Release Rate on the Mechanism of Geopolymer Gel Formation. *Chem. Mater.* **2010**, *22*, 5199–5208. [\[CrossRef\]](#)
43. Fernández-Jiménez, A.; Palomo, A.; Sobrados, I.; Sanz, J. The role played by the reactive alumina content in the alkaline activation of fly ashes. *Microporous Mesoporous Mater.* **2006**, *91*, 111–119. [\[CrossRef\]](#)
44. Rees, C.A.; Provis, J.L.; Lukey, G.C.; Van Deventer, J.S. In Situ ATR-FTIR Study of the Early Stages of Fly Ash Geopolymer Gel Formation. *Langmuir* **2007**, *23*, 9076–9082. [\[CrossRef\]](#) [\[PubMed\]](#)
45. Osswald, J.; Fehr, K.T. FTIR Spectroscopic Study on Liquid Silica Solutions and Nanoscale Particle Size Determination. *J. Mater. Sci.* **2006**, *41*, 1335–1339. [\[CrossRef\]](#)
46. Hajimohammadi, A.; Provis, J.L.; Van Deventer, J.S. One-Part Geopolymer Mixes from Geothermal Silica and Sodium Aluminate. *Ind. Eng. Chem. Res.* **2008**, *47*, 9396–9405. [\[CrossRef\]](#)
47. Zhang, Z.; Wang, H.; Provis, J.L.; Bullen, F.; Reid, A.; Zhu, Y. Quantitative kinetic and structural analysis of geopolymers. Part 1. The activation of metakaolin with sodium hydroxide. *Thermochim. Acta* **2012**, *539*, 23–33. [\[CrossRef\]](#)
48. Criado, M.; Fernández-Jiménez, A.; Palomo, A. Alkali activation of fly ash: Effect of the SiO<sub>2</sub>/Na<sub>2</sub>O ratio Part I: FTIR study. *Microporous Mesoporous Mater.* **2007**, *106*, 180–191. [\[CrossRef\]](#)
49. Criado, M.; Palomo, A.; Fernández-Jiménez, A. Alkali activation of fly ashes. Part 1: Effect of curing conditions on the carbonation of the reaction products. *Fuel* **2005**, *84*, 2048–2054. [\[CrossRef\]](#)
50. Lodeiro, I.G.; Macphée, D.E.; Palomo, A.; Fernández-Jiménez, A. Effect of alkalis on fresh C-S-H gels FTIR analysis. *Cem. Concr. Res.* **2009**, *39*, 147–153. [\[CrossRef\]](#)
51. Pan, X.; Shi, Z.; Shi, C.; Hu, X.; Wu, L. Interactions between inorganic surface treatment agents and matrix of Portland cement-based materials. *Constr. Build. Mater.* **2016**, *113*, 721–731. [\[CrossRef\]](#)
52. Simonsen, M.E.; Sønderby, C.; Li, Z.; Søgaard, E.G. XPS and FT-IR investigation of silicate polymers. *J. Mater. Sci.* **2009**, *44*, 2079–2088. [\[CrossRef\]](#)
53. Chen, W.; Li, B.; Wang, J.; Thom, N. Effects of alkali dosage and silicate modulus on autogenous shrinkage of alkali-activated slag cement paste. *Cem. Concr. Res.* **2021**, *141*, 106322. [\[CrossRef\]](#)

**Disclaimer/Publisher's Note:** The statements, opinions and data contained in all publications are solely those of the individual author(s) and contributor(s) and not of MDPI and/or the editor(s). MDPI and/or the editor(s) disclaim responsibility for any injury to people or property resulting from any ideas, methods, instructions or products referred to in the content.